



# Synchrotron X-ray radiographic investigations of liquid water transport behavior in a PEMFC with MPL-coated GDLs

J. Lee, J. Hinebaugh, A. Bazylak\*

Microscale Energy Systems Transport Phenomena Laboratory, Department of Mechanical & Industrial Engineering, Faculty of Applied Science & Engineering, University of Toronto, 5 King's College Road, Toronto, Ontario, Canada M5S 3G8

## HIGHLIGHTS

- Synchrotron X-ray radiography was used to visualize dynamic liquid water transport in a PEMFC.
- Breakthrough locations for PEMFCs with and without MPLs were compared.
- MPLs prevent the formation of large connected clusters of liquid water in the GDL.

## ARTICLE INFO

### Article history:

Received 1 August 2012  
Received in revised form  
17 October 2012  
Accepted 2 November 2012  
Available online 13 November 2012

### Keywords:

Polymer electrolyte membrane fuel cell  
Liquid water  
Water management  
Gas diffusion layer  
Synchrotron X-ray radiography  
Micro-porous layer

## ABSTRACT

Synchrotron X-ray radiography was employed to visualize the distribution of liquid water throughout an operating polymer electrolyte membrane fuel cell (PEMFC). The behavior of liquid water in the fuel cells assembled with and without micro-porous layers (MPLs) was compared. Through-plane images under various operating conditions combined with PEMFC performance revealed that, under wet conditions, the MPL was associated with an increased number of breakthrough locations, resulting in higher operating potentials. With these results, it is suggested that the MPL prevents liquid water from agglomerating into larger clusters at the catalyst layer/MPL interface, thereby reducing the number of blocked pathways for oxygen transport.

© 2012 Elsevier B.V. All rights reserved.

## 1. Introduction

Proper water management in the polymer electrolyte membrane fuel cell (PEMFC) is critical for achieving high, stable performance. Although the membrane must be hydrated to ensure effective proton conductivity, excess liquid water tends to accumulate in the gas diffusion layer (GDL) and flow fields, leading to mass transport limitations. It is commonly proposed that liquid water generated from chemical reactions at the catalyst layer (CL) is driven by capillary forces and percolates through the GDL into the flow fields [1,2]. Combined numerical and experimental results have indicated that liquid water accumulates in a tree-like pattern, and droplets are ejected into the flow channel [3,4]. Numerical studies have been performed with the goal to further understand

the relationship between water transport and the material characteristics of the GDL, such as porosity and hydrophobic treatment [5,6].

A micro-porous layer (MPL) is often employed between the CL and GDL to improve water management. An MPL is typically composed of carbon black and a hydrophobic material producing smaller pore sizes and higher hydrophobicity than in the GDL. Various numerical models and experiments have been proposed to understand phenomena by which MPLs affect liquid water distribution and transportation [1,2,7–20]. Qi and Kaufman [8] applied MPLs on various GDLs and found that water management was dominated by MPLs, which improved the overall performance. Nam and Kaviany [2] and Pasaogullari and Wang [9] developed half-cell models to predict reduced liquid water saturation in the cathode by enhanced water removal due to the high capillary pressures associated with the pores of the MPL. However, full fuel cell models, involving both anode and cathode, by Pasaogullari et al. [11] and Weber [21] hypothesized that the hydraulic pressure gradient

\* Corresponding author. Tel.: +1 416 946 5031; fax: +1 416 978 7753.  
E-mail address: [abazylak@mie.utoronto.ca](mailto:abazylak@mie.utoronto.ca) (A. Bazylak).

across the membrane induces liquid water transport from cathode to anode, which is known as back diffusion. Experimental results [13,16,19] supported enhanced back diffusion, proposing that MPLs act as capillary barriers that reduce the ion transfer resistance of the membrane. However, Atiyeh et al. [12] performed water balance analyses on an operating cell, and concluded that an MPL at the cathode did not have any impact on back diffusion. Gostick et al. [15] measured the water saturation and capillary pressure at breakthrough in GDLs with and without an MPL, and they suggested that an MPL decreased the accessibility of water at the GDL inlet face during percolation, resulting in decreased saturation. Nam et al. [14] established mathematical approach to water morphology control by MPLs. The number and size of liquid water droplets evolved in the catalyst–GDL interface were reduced, thereby lowering the saturation in the GDL. In addition, Lu et al. [17] discovered that the MPL stabilizes water breakthrough passages effectively lowering saturation. Recently, the significance of two phase transport phenomena in the GDL has been proposed [22–26]. In certain conditions, vapor phase transport dominates and solely facilitates product water removal from the catalyst layer to the flow channel. Owejan et al. [24] proposed that the role of the cathodic MPL was to prevent water vapor condensation at the CL–GDL interface. However, the underlying mechanisms causing improvement in water management by employing MPLs have not been thoroughly studied through in-situ visualizations.

There have been several efforts to visualize water content in an operating PEMFC, as highlighted in a review by Bazylak [27]. Jiao et al. [28] and Zhan et al. [29] replaced the traditional metallic components of a fuel cell with transparent materials in order to visualize the eruptive transport mechanism of water droplets from the GDL to the flow channel with optical microscopy. However, Jiao et al. [28] and Zhan et al. [29] focused on the surface of the GDL, and their fuel cell modifications may have had significant impacts on the contact resistance, thermal distribution, and compression of the fuel cell. Neutron radiography has proven to be valuable in visualizing liquid water distributions in the GDL [20,30–33]. Despite its sensitivity for detecting hydrogen-containing molecules, neutron radiography has been generally limited to spatial and temporal resolutions of 25  $\mu\text{m}$  and 5.4 s, respectively [27]. Murakawa et al. [33] successfully reduced the pixel size down to 6.6  $\mu\text{m}$  at 10 s per frame by employing a borescope system, and they averaged five consecutive images to address noise concerns. Preston et al. [34] developed neutron radiography methods to achieve a spatial resolution 13  $\mu\text{m}$  for PEMFC investigations. Tremendous progress has been made in the refinement of neutron radiography methods to investigate PEMFCs, such as by Mishler et al. [20]; however, due to the somewhat limited accessibility of neutron imaging to other

researchers, complementary methods such as synchrotron X-ray radiography are valuable.

Recently, synchrotron X-ray radiography has been demonstrated by a number of researchers as a promising method for visualizing multiphase flow within an operating PEMFC [35–40]. High spatial and temporal resolutions down to 0.7  $\mu\text{m}$  at 1 s per frame have been key to providing insight into the distribution and transport of liquid water in an operating PEMFC [39]. Manke et al. [40] utilized synchrotron radiography to image liquid water in a PEMFC and observed the dynamic behavior of Haines' jumps through the eruptive transport behavior of droplets emerging from the GDL into the flow channel. Hartnig et al. [39] utilized synchrotron radiography to visualize the cross-section of the cell, and the water saturation profiles across the GDL, MPL, channel, and interfaces were quantified for a range of current densities. Similarly, Lee et al. [37] performed an in-plane visualization to obtain cross-sectional water profiles as a function of time.

In this study, synchrotron X-ray radiographic imaging was employed to dynamically visualize the distribution of liquid water in a PEMFC to investigate the effect of the MPL on liquid water transport behavior. A PEMFC was designed so that the X-ray beam was not prohibitively attenuated by traditional metallic components. The overall performance, liquid water distribution, and breakthrough density of the GDL were determined for an operating PEMFC using Toray TGP-H-090 GDLs with and without MPLs, where breakthrough corresponds to the first formation of a cluster of liquid water invaded pores that spans the MPL side of the GDL through to the gas channel/GDL interface.

## 2. Experimental setup

A single cell PEMFC with an active area of 25  $\text{cm}^2$  was designed for through-plane imaging with three holes (1.27 cm diameter) through the metallic end plates (Fig. 1). These holes were partially extended through a portion of the graphite flow field, resulting in shallow pockets (0.89 cm depth with 0.381 cm of graphite remaining). Gas channels on the graphite flow field with 1 mm depth were not disturbed by the pockets. While it was not expected that these modifications would impact the cell compression, further investigations will be needed to determine the effect on the temperature distribution. The viewing pockets facilitated sufficient X-ray beam penetration and maximized attenuation contrast between the liquid water and fuel cell components (Fig. 1). The viewing pocket closest to the outlet was exclusively investigated in the present study, since the outlet region featured the most significant water management issues. The temperature distribution was assumed to be uniform and not affected by the viewing

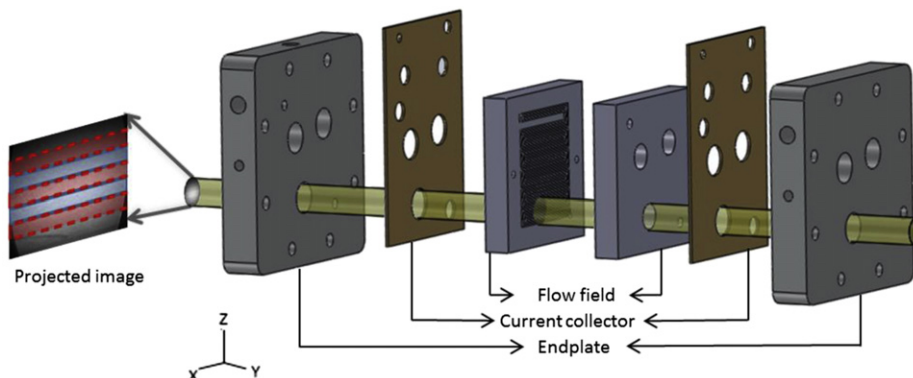


**Fig. 1.** Schematic showing the components of the fuel cell with an active area of 25  $\text{cm}^2$ . The path of the X-ray beam (yellow) is directed in the y-direction, through the lower viewing hole, which was the focus of this investigation. The projected image is magnified to the left.

pockets. A triple serpentine flow field design was employed for both the anodic and cathodic plates, and the anodic flow field pattern was vertically offset by the width of a single channel to elucidate electrode-specific water accumulation. The resulting staggered flow channel geometry can be seen in Fig. 2.

Catalyst coated membranes (Ion Power, New Castle, USA) of Nafion N115 with platinum loadings of  $0.3 \text{ mg cm}^{-2}$  on each electrode were employed. The fuel cells were built with Toray paper GDLs (TGP-H-090) treated with polytetrafluoroethylene (PTFE) loadings of 10 wt.%, created both with and without MPLs. The assembly pressure applied to each GDL was calibrated with pressure film to ensure uniform, repeatable compression. All cell tests were performed with a Scribner 850e test station (Scribner Associates Inc., Southern Pines NC). The cell temperature was held at  $75^\circ\text{C}$ , and the reactants (hydrogen and air) were maintained at 65% relative humidity. During Sections (B)–(D), the stoichiometric ratios were set to either 1.1 or 1.4 for the cathode and 2.8 or 6.6 for the anode, while the current density was held at  $0.6 \text{ A cm}^{-2}$ . Ambient pressure was maintained at the outlets. Although these stoichiometric ratios are not realistic or ideal for practical fuel cell stacks, it is important to note that the authors specifically chose to operate the fuel cell under these conditions to instigate flooding to allow for the observation of dynamic liquid water accumulation and transport. These operating conditions were based on our previous experiments at the same facility [41], which were tested prior to the experiment to ensure repeatability.

All experiments described in this work were performed at the Biomedical Imaging and Therapy Beam line (05B1-1) of the Canadian Light Source Inc. (CLS) (Saskatoon, Canada). The CLS is a third generation 2.9 GeV synchrotron facility. Through-plane absorption imaging was performed, meaning the beam was directed perpendicular to the plane of the fuel cell. An energy level of 18.1 keV was selected through manual calibration for optimal detection of liquid water at this facility. The temporal resolution was  $\sim 3 \text{ s}$  per frame, and the effective spatial resolution was  $8\text{--}10 \mu\text{m}$ . The schematic of the experimental setup is illustrated in Fig. 3.

The raw image consists of grey-scale values as seen in the projected image of Fig. 1. The accumulation of liquid water was distinguished from the stationary components of the PEMFC through the application of Beer–Lambert’s law to the raw images [37]. Beer–Lambert’s law correlates the intensity of the attenuated X-ray to

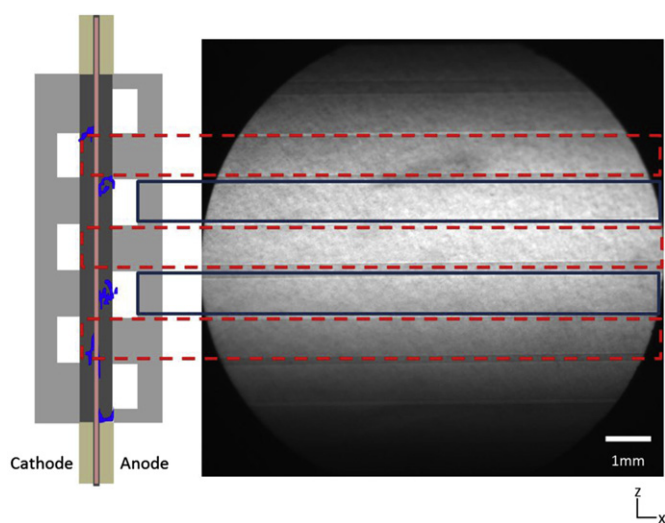


Fig. 2. Schematic illustrating the offset positioning of the anodic (black, solid) and cathodic (red, dashed) flow channels (1 mm). (For interpretation of the references to colour in this figure legend, the reader is referred to the web version of this article.)

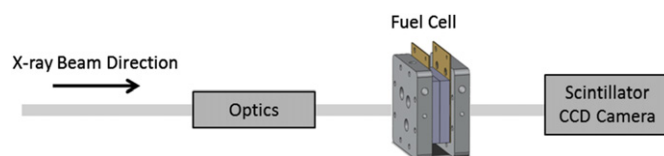


Fig. 3. Schematic of experimental setup at the synchrotron facility.

the thickness of the material traversed by the beam. During all visualizations, the fuel cell and all surrounding hardware remained stationary. Only mass transport within the fuel cell contributed to variations in the attenuated X-ray beam. In particular, the formation and motion of liquid water within the fuel cell was reflected in the normalized radiographic images. The “dry-state” image, obtained at open circuit voltage (OCV), was employed to normalize subsequent “wet-state” images that contained liquid water under a current density that ranged from  $0.2$  to  $0.6 \text{ A cm}^{-2}$ . Raw images were normalized in such a way as to account for beam fluctuations with the procedure described in detail by Hinebaugh et al. [42].

### 3. Results

Two single cell PEMFCs were assembled and tested under conditions of current control, under varying stoichiometric ratios. The first cell was assembled without an MPL coating on either GDL, and the second cell had an MPL coating on both anodic and cathodic GDLs. Section (A) of the operating sequence shown in Fig. 4 depicts the performance of both fuel cells at 0 (OCV), 0.2, 0.4 and  $0.6 \text{ A cm}^{-2}$  at fixed flow rates, 0.7 and  $1.12 \text{ slpm}$  for anode and cathode, respectively. In Section (A), the current was increased in a stepwise manner at  $0.2 \text{ A cm}^{-2}$  at 5 min per step, and throughout this section the stoichiometric ratios were set to be greater than 10 to establish dry baseline conditions. In Sections (B)–(D), the current density was held constant at  $0.6 \text{ A cm}^{-2}$ , and the stoichiometric ratios were systematically adjusted to  $\lambda_c = 1.4, 1.1, 1.4$  and  $\lambda_a = 6.6, 6.6, 2.8$ , respectively, as shown in Fig. 4, where subscript *c* refers to the cathode and *a* refers to the anode. In Sections (B) and (C), the stoichiometric ratios were chosen to provide longer residence times for liquid water. In Section (D), the anodic stoichiometric ratio was further decreased from 6.6 to 2.8 to investigate the effect of liquid water accumulation in the fuel cell. A relatively high anodic stoichiometric ratio was adapted throughout the experiment such that anodic and cathodic volumetric flow rates were similar.

Synchrotron radiographic images presented in Fig. 5 were obtained near the outlet region of the PEMFC without MPLs (left) and with MPLs (right) at times highlighted by dashed lines in Fig. 4. Cathodic channels are labeled as ‘*C<sub>i</sub>*’, and anodic channels as ‘*A<sub>i</sub>*’, where *i* = 1, 2, 3 refers to the channel number. The irregular regions highlighted in Boxes 1–3 of Fig. 5(l) will be addressed below in the Discussion section.

#### 3.1. High anode and cathode stoichiometric ratios (Sections A and B)

In Section (A) of Fig. 4, excess liquid water was not observed in either fuel cell. It is important to note that some water must be present in the system during PEMFC operation, since the membrane requires hydration, and water is generated via the electrochemical reactions that drive the fuel cell. However, in Section (A), excessive reactant flows (stoichiometric ratios  $> 10$ ) offered a balance between water production and removal rates, thereby keeping the fuel cell relatively dry. Water produced in the cathode as a result of the chemical reaction evaporated and diffused through the GDL to the flow channel in the gas phase or was imbibed by the membrane. Although the high stoichiometric ratios

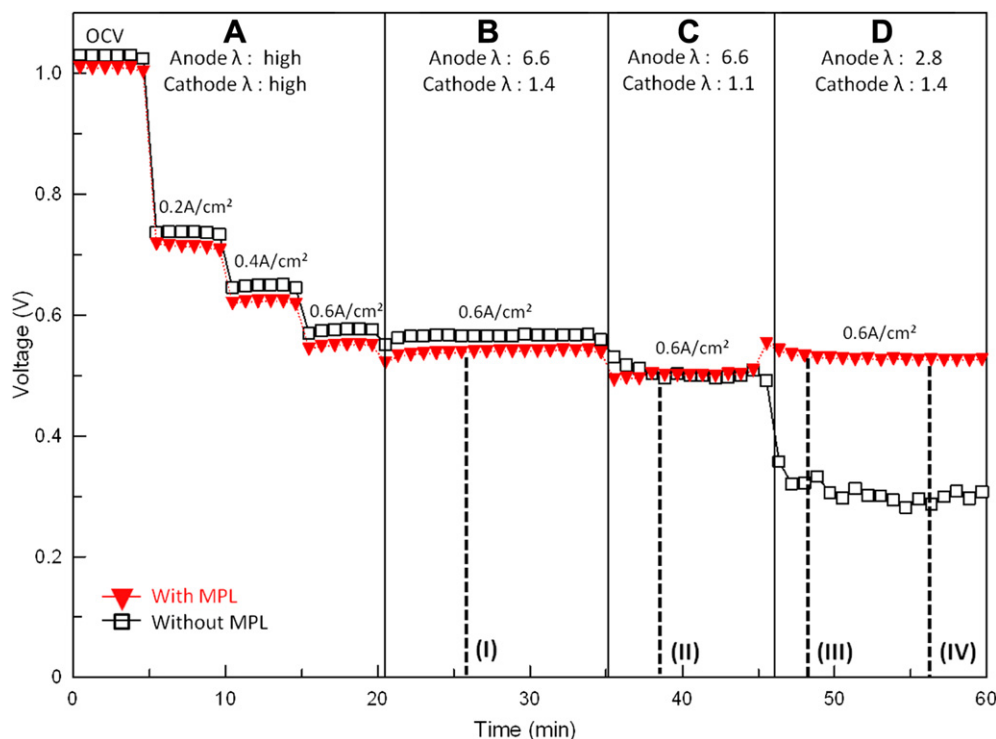


**Fig. 4.** Performance comparison of two PEMFCs employing TGP-H-090: one with MPLs (red) and without (black). Performance is compared at prescribed currents and stoichiometric ratios, (A)–(D) classifies operating conditions; dashed lines (I)–(IV) correspond to sequential images in Fig. 5. (For interpretation of the references to colour in this figure legend, the reader is referred to the web version of this article.)

facilitated effective water management and reasonable performance of the cell, these operating conditions would not be ideal in practice due to wasted fuel and high parasitic losses.

In the fuel cell without MPLs, water droplets started to form approximately 4 min after decreasing the anodic and cathodic stoichiometric ratios in Section (B) of Fig. 4. These sparsely located water droplets evolved on the edges of the cathodic channels (Fig. 5(I) C<sub>2</sub> and C<sub>3</sub>), after which, no new breakthrough locations were found. Water droplets repeatedly grew, were carried away by water slugs, and re-emerged at the same breakthrough locations. In contrast, distinct liquid water droplets did not appear in the channels of the fuel cell with MPLs; however, as shown in Fig. 5(I) (right), liquid water was homogeneously distributed over the entire viewing area. No distinct droplets were seen throughout Sections (A) and (B), the performance of the fuel cell without MPLs slightly surpassed that of the fuel cell with MPLs by approximately 50 mV; however, both fuel cells held relatively stable potentials throughout the experiment.

### 3.2. Low cathode stoichiometric ratio (Section C)

In Section (C) of Fig. 4, the cathodic stoichiometric ratio was reduced from 1.4 to 1.1. The potential of the cell without MPLs gradually declined after the initial step decrease in potential. In the cell without MPLs, the number of breakthrough locations and size of droplets remained fairly consistent, compared to the previous section. Occasionally, a slug of water, as seen in C<sub>3</sub> of Fig. 5(II) (left), swept through the channel and removed most droplets in its path. Following slug formation and departure, droplets continued to emerge at the same breakthrough locations. In contrast, in the fuel cell with MPLs, water droplets started to evolve in the cathodic channel (C<sub>3</sub>), as highlighted with a box in Fig. 5(II) (right). The liquid water distribution in the fuel cell with MPLs closely resembled the previous operating conditions in Fig. 5(I) (right). The potential of

the fuel cell without MPLs was no longer higher than the potential of the fuel cell with MPLs.

### 3.3. Low anode stoichiometric ratio (Section D)

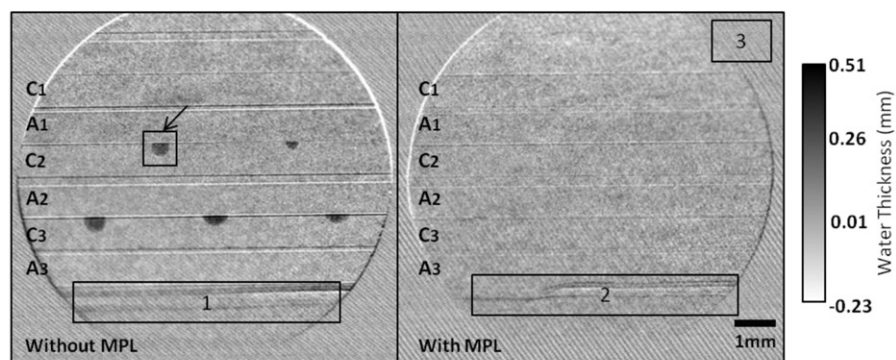
In Section (D), the anodic stoichiometric ratio was reduced to 2.8 and the cathodic stoichiometric ratio was raised to 1.4 (see Fig. 4). Within 2 min, a large number of droplets began to form in the cathodic channels of the fuel cell with MPLs, as seen in Fig. 5(III) (right). Uniformly distributed droplets of equivalent size at the initial stage of development appeared, though some droplets grew at faster rates, sometimes agglomerating with surrounding droplets (Fig. 5(IV) (right)). Haines' jumps [39,43,44], which describe the repetitive eruptive transport mechanism of water droplets into the channel, were also observed in Section (D). It was assumed that the formation of water droplets led to small potential fluctuations; however, these fluctuations did not significantly affect the performance of the cell, which was comparable to the performance seen in Section (B) (higher anodic stoichiometric ratio). In contrast, under the same operating conditions, the fuel cell without MPLs resulted in a reduced potential (by 0.3 V) compared to the setting with a higher anode stoichiometric ratio (Section (C)). The number of breakthrough locations slightly increased in comparison with the previous settings of Section (B). However, the cell with MPLs exhibited a higher number of new breakthrough locations and the rapid ejection of liquid water into the channels compared to the cell without MPLs.

## 4. Discussion

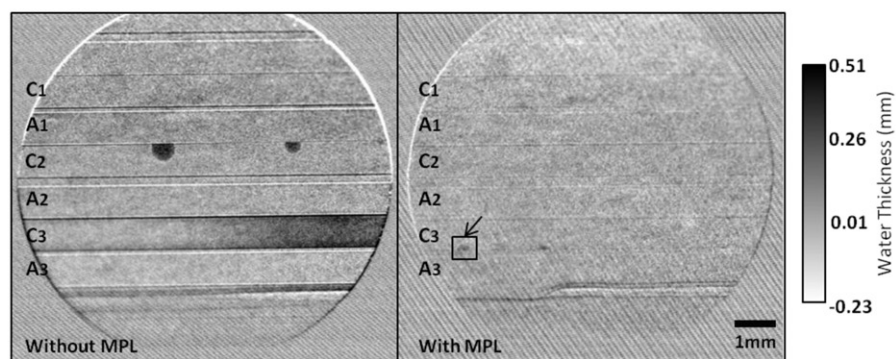
### 4.1. Artifacts

The irregular regions highlighted in Boxes 1 and 2 in Fig. 5(I) are horizontally oriented artifacts caused by a defect on the

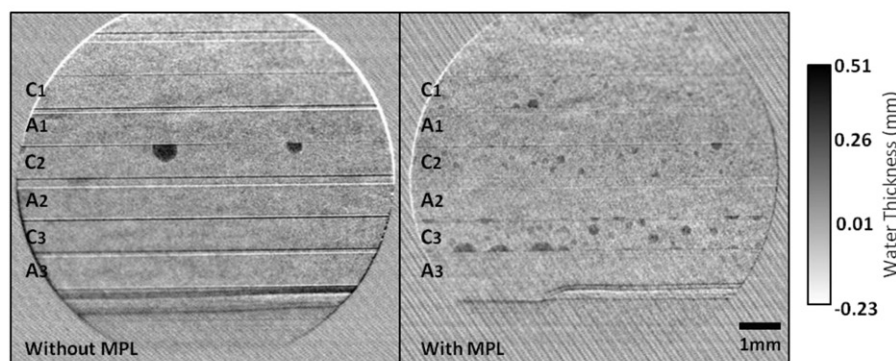




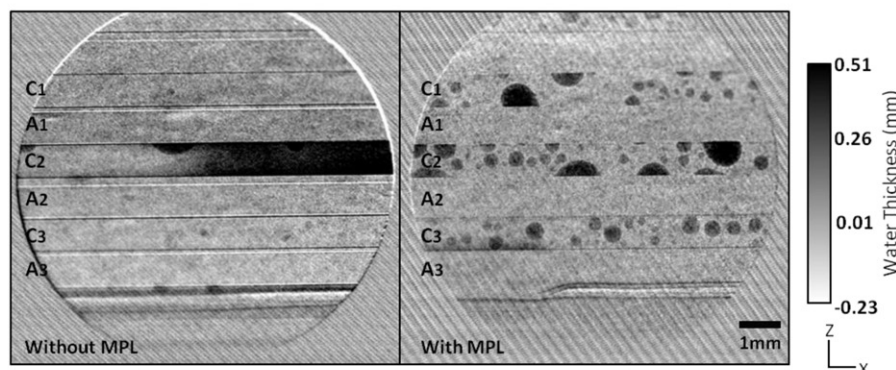
(I)  $0.6 \text{ A cm}^{-2}$ , anodic stoichiometric ratio: 6.6, cathodic stoichiometric ratio: 1.4, boxes 1 and 2 highlight artifacts on a monochromator. The Box 3 represents diagonal artifacts, and the box with an arrow indicates a droplet evolving.



(II)  $0.6 \text{ A cm}^{-2}$ , anodic stoichiometric ratio: 6.6, cathodic stoichiometric ratio: 1.1. The highlighted box indicates a droplet evolving in the cathodic channel.



(III)  $0.6 \text{ A cm}^{-2}$ , anodic stoichiometric ratio: 2.8, cathodic stoichiometric ratio: 1.4



(IV)  $0.6 \text{ A cm}^{-2}$ , anodic stoichiometric ratio: 2.8, cathodic stoichiometric ratio: 1.4

**Fig. 5.** Synchrotron X-ray radiographic images highlighting the appearance of liquid water at various times identified in Fig. 4: Left Toray TGP-H-090 and right TGP-H-090 with MPLs.

monochromator. Regularly spaced diagonal lines, highlighted in Box 3 in Fig. 5(I), are artifacts caused by the noise associated with the charge-coupled device (CCD) camera. Artifacts were also found at the edges of the viewing holes and flow channels, and these artifacts became more distinct at later stages of the experiment (I)–(IV). These artifacts may have been caused by a micrometer-scale movement of the PEMFC during operation. The intensity of the beam was not uniform throughout the field of view, and the center region was initially brightest. The location of the brightest region was subjected to fluctuation due to an uneven temperature distribution in the monochromator, and this combined with overall tendency of the brightest region moving downward led to difficulties in quantifying water saturation in GDLs [41].

#### 4.2. Effects of MPL under dry conditions

The fuel cell without MPLs exhibited higher potentials by 50 mV compared to that with MPLs at all currents in Section (A) of Fig. 4. However, this variation between the MPL and non-MPL containing fuel cells is not statistically relevant enough to conclude on the effect of the MPL in this regime. Each fuel cell was run three times, and the voltage difference between runs was 10 to 25 mV under dry conditions. It is possible that the fuel cells were not completely dried between each experiment providing an offset to initial ionic resistance of the membrane. Further investigations such as electrochemical impedance spectroscopy are required to investigate the roles of the MPL during these dry-state conditions.

#### 4.3. Effects of MPL under wet conditions

The impact of the MPL on water management is most notably seen at high current densities and low stoichiometric ratios. In Section (D), where a 0.3 V drop in performance accompanied the change in stoichiometric ratios, only a few new droplets appeared in the fuel cell without MPLs, even after several minutes. Additionally, a noticeable increase in droplet size was not observed. On the other hand, the fuel cell with MPLs showed a sudden increase in the sizes and number of breakthrough locations in Section (D) (Fig. 4), and despite this increase in water droplet appearance, the operating potential remained relatively unchanged from Section (C). This indicates that in the fuel cell without MPLs, liquid water flooding in the GDL led to reactant mass transport limitations, while the accumulation of liquid water in the fuel cell with MPLs did not lead to significant mass transport limitations. The liquid water saturations of fuel cells without and with MPLs are

illustrated in Fig. 6. Both images were taken after the conclusion of Section (D), in which fuel cells were at OCV with high flow rates to remove water droplets in the flow channel. Most water droplets in the fuel cell with MPLs were successfully carried away by water slugs within 6 s (less than 2 frames), whereas in the fuel cell without MPLs, some droplets remained, as no up-stream slug formed. To improve image clarity, four consecutive images immediately after droplet removal were averaged, and the brightness and contrast level was adjusted to elucidate residual liquid water in the system. The artifacts causing negative water thickness became more noticeable here than in Fig. 5 due to the high contrast and increased beam position movement towards the end of the experiments. As seen in Fig. 6, the overall water saturation in the fuel cell without MPLs is higher than with MPLs. What might initially seem like a counter-intuitive result can be explained by the hypothesis that while liquid water primarily occupied the pores of the CL and GDL in the fuel cell without MPLs (thereby blocking reaction sites), liquid water primarily occupied the flow fields of the fuel cell with MPLs. Furthermore, it can be concluded that less net liquid water was accumulating in the visualized region of the cell without MPLs. We assume this is the result of localized flooding of the GDL, preventing high current densities in these regions.

The MPL has smaller pores and is potentially more hydrophobic than the GDL. Additionally, the MPL pores are more evenly distributed compared to the GDL [14]. It is hypothesized that these MPL properties may lead to a more uniform distribution of liquid water at the CL/MPL interface, before breakthrough occurs. Once the necessary amount of liquid water accumulates at the CL/MPL interface to reach a critical breakthrough pressure, liquid water penetrates the MPL and reaches the MPL–GDL interface, where secondary breakthrough occurs and droplets are expelled from the GDL into the flow channel [14]. The high number of breakthrough locations on the top surface of the GDL (with an MPL) may indicate an effective removal of liquid water from the system, thus preventing flooding [17]. On the other hand, the GDL (without an MPL) is highly prone to liquid water flooding (high saturation levels), as water may occupy large pores in large well-connected clusters within the GDL before percolating through to breakthrough. The resulting impact of the MPL on the liquid water accumulation in the GDL is depicted in the schematic shown in Fig. 7.

#### 4.4. Future consideration

The impact of synchrotron X-rays on an operating fuel cell has been addressed by other authors, but this impact inquires further

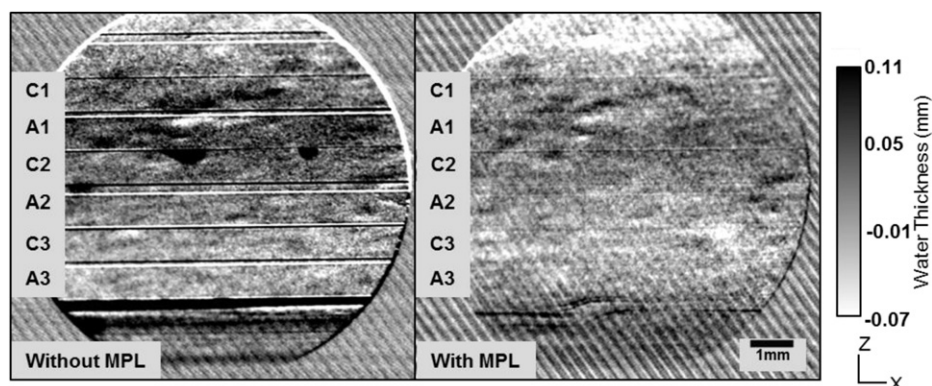
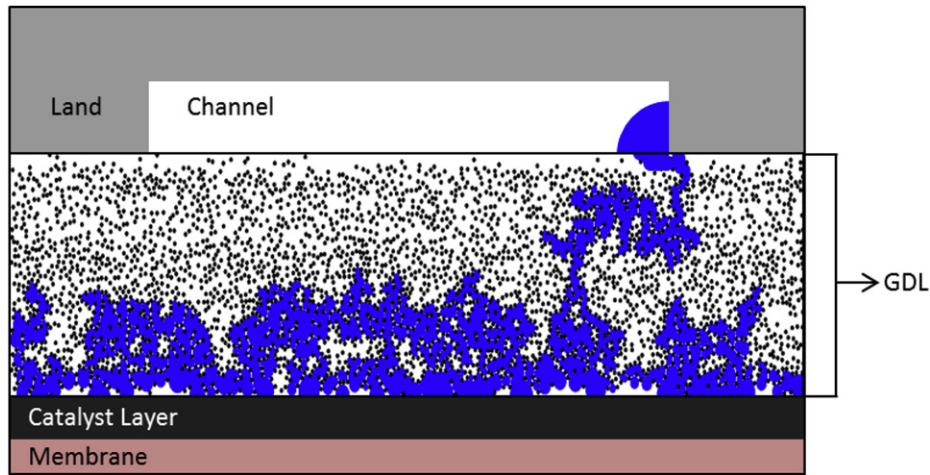
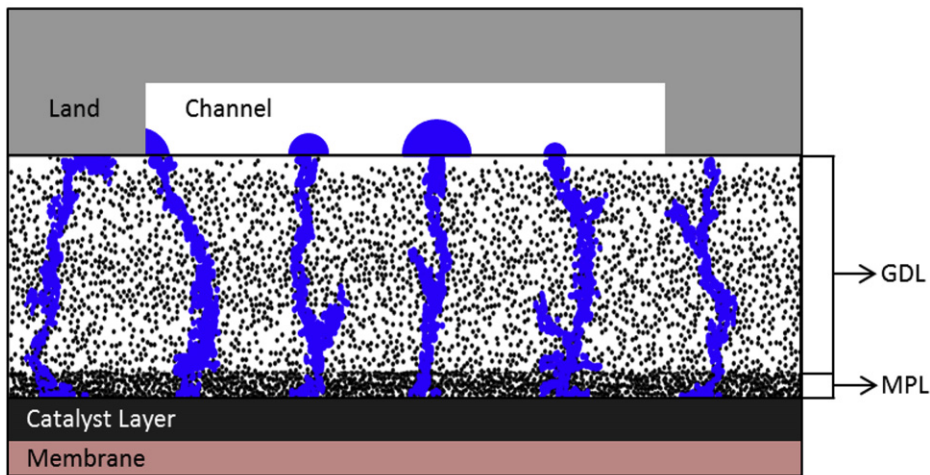


Fig. 6. Comparison of liquid water saturations in Toray TGP-H-090 (left) and TGP-H-090 with MPLs (right) at OCV and 1 lpm.





(I) Liquid water transport in a GDL without MPLs



(II) Liquid water transport in a GDL with MPLs

Fig. 7. Comparison of liquid water evolution and transport in a GDL with and without MPLs.

investigation. Schneider et al. [38] investigated liquid water in a miniaturized fuel cell by synchrotron X-ray micro-computed tomography, where the entire fuel cell was exposed to a synchrotron beam. The performance rapidly decayed with an exposure to the beam resulting in a failure of the system. Similarly, Eller et al. [45] and Roth et al. [46] investigated the impact of the synchrotron beam during X-ray tomography imaging. It was found that after a certain period of synchrotron radiation, the mechanical properties and wettability of fuel cell materials degraded [46]. In the present study, performance degradation was not noticeable, perhaps because the area exposed to synchrotron radiation was relatively small compared to the active area or because the beam intensity was not comparable in the above studies. It is also possible that the remaining portion of the graphite flow field behaved as a shield to the inner components. However, it is necessary to identify the impact of the synchrotron beam on fuel cell components (i.e. decomposition of PTFE coating on GDLs, catalyst poisoning and PEM degradation [38,46]) that alters water behavior in the fuel cell, as it may influence the observed phenomena in practical operation. In our future studies, we will investigate the degradation effect of the synchrotron X-ray further. The viewing

pockets may have affected the boundary temperature, and the attenuated X-ray beam could have also heated the surface. Further investigation is required to isolate the impact on the temperature distribution by these parameters.

We have provided an isothermal explanation of the observed phenomena, assuming all liquid water must percolate through the GDL and MPL. However, this is a simplified explanation, as phase change may have a significant role to play in the PEMFC, as discussed by various authors [22–26].

Artifacts and noise caused by beam can be minimized by placing a combination of filters in the beam path. Details can be found in Ref. [41].

## 5. Conclusion

In this study, the effect of an MPL on the behavior of liquid water in an operating PEMFC was investigated with through-plane synchrotron X-ray radiography. Results indicate that the MPL improves the performance and reliability of the fuel cell during wet conditions. At high current density operation (under low stoichiometric ratios), the results suggest that the MPL prevented the flooding of the porous

layers. In-situ visualizations of liquid water were provided to support the hypothesis of capillary flow transport proposed by Refs. [2,9,11,14–17,19,21]. This beneficial behavior of the MPL may be attributed to the nano-sized pores that led to a reduction in GDL saturation, reduced liquid water cluster sizes, and overall improvement in liquid water removal.

## Acknowledgments

The authors would like to acknowledge the generous assistance of Dr. George Belev and Dr. Tomasz Wysokinski at the Canadian Light Source, in Saskatoon, SK, Canada. The authors would also like to thank Mr. Pradyumna Challa for his support with the experiments at the Canadian Light Source. Jason Scribner and Scribner Associates Inc., are also gratefully acknowledged for their generous use of their fuel cell testing equipment. Research described in this paper was performed at the Canadian Light Source, which is supported by the Natural Sciences and Engineering Research Council of Canada, the National Research Council Canada, the Canadian Institutes of Health Research, the Province of Saskatchewan, Western Economic Diversification Canada, and the University of Saskatchewan. Financial support to the authors from The Natural Sciences and Engineering Research Council of Canada (NSERC), Canada Foundation for Innovation (CFI), and University of Toronto are also gratefully acknowledged.

## References

- [1] C. Lim, C.Y. Wang, *Electrochim. Acta* 49 (2004) 4149–4156.
- [2] J.H. Nam, M. Kaviani, *Int. J. Heat Mass Transf.* 46 (2003) 4595–4611.
- [3] P.K. Sinha, C. Wang, *Electrochim. Acta* 52 (2007) 7936–7945.
- [4] S.P. Kuttanikkad, M. Prat, J. Pauchet, *J. Power Sourc.* 196 (2011) 1145–1155.
- [5] J. Hinebaugh, Z. Fishman, A. Bazylak, *J. Electrochem. Soc.* 157 (2010) B1651–B1657.
- [6] J.H. Chun, K.T. Park, D.H. Jo, S.G. Kim, S.H. Kim, *Int. J. Hydrogen Energy* 36 (2011) 1837–1845.
- [7] G.J.M. Janssen, M.L.J. Overvelde, *J. Power Sourc.* 101 (2001) 117–125.
- [8] Z. Qi, A. Kaufman, *J. Power Sourc.* 109 (2002) 38–46.
- [9] U. Pasaogullari, C. Wang, *Electrochim. Acta* 49 (2004) 4359–4369.
- [10] A.Z. Weber, J. Newman, *J. Electrochem. Soc.* 152 (2005) A677–A688.
- [11] U. Pasaogullari, C. Wang, K.S. Chen, *J. Electrochem. Soc.* 152 (2005) A1574–A1582.
- [12] H.K. Atiyeh, K. Karan, B. Peppley, A. Phoenix, E. Halliop, J. Pharoah, *J. Power Sourc.* 170 (2007) 111–121.
- [13] D. Spornjak, A.K. Prasad, S.G. Advani, *J. Power Sourc.* 170 (2007) 334–344.
- [14] J.H. Nam, K. Lee, G. Hwang, C. Kim, M. Kaviani, *Int. J. Heat Mass Transf.* 52 (2009) 2779–2791.
- [15] J.T. Gostick, M.A. Ioannidis, M.W. Fowler, M.D. Pritzker, *Electrochem. Commun.* 11 (2009) 576–579.
- [16] T. Kim, S. Lee, H. Park, *Int. J. Hydrogen Energy* 35 (2010) 8631–8643.
- [17] Z. Lu, M.M. Daino, C. Rath, S.G. Kandlikar, *Int. J. Hydrogen Energy* 35 (2010) 4222–4233.
- [18] F. Weng, C. Hsu, M. Su, *Int. J. Hydrogen Energy* 36 (2011) 13708–13714.
- [19] T.C. Yau, M. Cimenti, X. Bi, J. Stumper, *J. Power Sourc.* 196 (2011) 9437–9444.
- [20] J. Mishler, Y. Wang, R. Mukundan, J. Spendelow, D.S. Hussey, D.L. Jacobson, R.L. Borup, *Electrochim. Acta* 75 (2012) 1–10.
- [21] A.Z. Weber, *J. Power Sourc.* 195 (2010) 5292–5304.
- [22] M.C. Hatzell, A. Turhan, S. Kim, D.S. Hussey, D.L. Jacobson, M.M. Mench, *J. Electrochem. Soc.* 158 (2011) B717–B726.
- [23] D.A. Caulk, D.R. Baker, *J. Electrochem. Soc.* 157 (2010) B1237–B1244.
- [24] J.P. Owejan, J.E. Owejan, W. Gu, T.A. Trabold, T.W. Tighe, M.F. Mathias, *J. Electrochem. Soc.* 157 (2010) B1456–B1464.
- [25] K.T. Cho, M.M. Mench, *J. Power Sourc.* 195 (2010) 3858–3869.
- [26] K.T. Cho, M.M. Mench, *J. Power Sourc.* 195 (2010) 6748–6757.
- [27] A. Bazylak, *Int. J. Hydrogen Energy* 34 (2009) 3845–3857.
- [28] K. Jiao, J. Park, X. Li, *Appl. Energy* 87 (2010) 2770–2777.
- [29] Z. Zhan, C. Wang, W. Fu, M. Pan, *Int. J. Hydrogen Energy* 37 (2012) 1094–1105.
- [30] Y.S. Chen, H. Peng, D.S. Hussey, D.L. Jacobson, D.T. Tran, T. Abdel-Baset, M. Biernacki, *J. Power Sourc.* 170 (2007) 376–386.
- [31] R. Satija, D.L. Jacobson, M. Arif, S.A. Werner, *J. Power Sourc.* 129 (2004) 238–245.
- [32] H. Markötter, I. Manke, R. Kuhn, T. Arlt, N. Kardjilov, M.P. Hentschel, A. Kupsch, C. Lange, C. Hartnig, J. Scholta, J. Banhart, *J. Power Sourc.* 219 (2012) 120–125.
- [33] H. Murakawa, D. Wada, K. Sugimoto, H. Asano, N. Takenaka, R. Yasuda, *Nucl. Instrum. Meth. Phys. Res.* 651 (2011) 286–289.
- [34] J. Preston, U. Pasaogullari, D.S. Hussey, D.L. Jacobson, *ECS Trans.* 41 (2011) 319.
- [35] P. Krüger, H. Markötter, J. Haußmann, M. Klages, T. Arlt, J. Banhart, C. Hartnig, I. Manke, J. Scholta, *J. Power Sourc.* 196 (2011) 5250–5255.
- [36] H. Markötter, I. Manke, P. Krüger, T. Arlt, J. Haußmann, M. Klages, H. Riesemeier, C. Hartnig, J. Scholta, J. Banhart, *Electrochem. Commun.* 13 (2011) 1001–1004.
- [37] S. Lee, S. Kim, G. Park, C. Kim, *Int. J. Hydrogen Energy* 35 (2010) 10457–10463.
- [38] A. Schneider, C. Wieser, J. Roth, L. Helfen, J. Power Sourc. 195 (2010) 6349–6355.
- [39] C. Hartnig, I. Manke, R. Kuhn, S. Kleinau, J. Goebbels, J. Banhart, *J. Power Sourc.* 188 (2009) 468–474.
- [40] I. Manke, C. Hartnig, M. Gruenerbel, W. Lehnert, N. Kardjilov, A. Haibel, A. Hilger, J. Banhart, H. Riesemeier, *Appl. Phys. Lett.* 90 (2007) 174105.
- [41] J. Hinebaugh, J. Lee, A. Bazylak, *J. Electrochem. Soc.* 159 (2012) F826–F830.
- [42] J. Hinebaugh, P.R. Challa, A. Bazylak, *J. Synchrotron Rad.* 19 (2012) 994–1000.
- [43] C. Hartnig, I. Manke, R. Kuhn, N. Kardjilov, J. Banhart, W. Lehnert, *Appl. Phys. Lett.* 92 (2008) 134106.
- [44] I. Manke, C. Hartnig, M. Gruenerbel, J. Kaczerowski, W. Lehnert, N. Kardjilov, A. Hilger, J. Banhart, W. Treimer, M. Strobl, *Appl. Phys. Lett.* 90 (2007) 184101.
- [45] J. Eller, T. Rosen, F. Marone, M. Stapanoni, A. Wokaun, F.N. Büchi, *J. Electrochem. Soc.* 158 (2011) B963–B970.
- [46] J. Roth, J. Eller, F.N. Büchi, *J. Electrochem. Soc.* 159 (2012) F449–F455.